JGR Oceans

Key Points:

- Variation of modal ice thickness is characterized by thermodynamic ice growth in the north Ross Sea and ice advection in the south Ross Sea
- Sea ice in the southeast Ross Sea was significantly deformed in 2019–2020 due to the inflow of thick ice and convergent ice drift
- Strong southerly wind associated with the Amundsen Sea Low decreased sea ice deformation in the southeast Ross Sea in 2021 and 2022

Supporting Information:

Supporting Information may be found in the online version of this article.

Correspondence to:

H. Xie,
hongjie.xie@utsa.edu

Thermodynamic and Dynamic Variations in Sea Ice Thickness of the Ross Sea, Antarctica, Driven by Atmospheric Circulation

Younghyun Koo[1,2] ⓘ**, Hongjie Xie**[1] ⓘ**, and Stephen F. Ackley**[1,3] ⓘ

[1]Department of Earth and Planetary Sciences, University of Texas at San Antonio, San Antonio, TX, USA, [2]National Snow and Ice Data Center, Cooperative Institute for Research in Environmental Sciences, University of Colorado Boulder, Boulder, CO, USA, [3]Center for Advanced Measurements in Extreme Environments (CAMEE), University of Texas at San Antonio, San Antonio, TX, USA

Abstract Atmospheric circulation has significant impacts on sea ice drifting patterns and mass balance, as wind drag induces pressure ridges and leads on the sea ice surface. In this study, the spatiotemporal distributions of these dynamic sea ice deformation features in the Ross Sea are examined using ICESat-2 (IS2) ATL10 freeboard data (2019–2022). The temporal variation of the modal sea ice thickness (SIT), caused by thermodynamic ice growth and sea ice advection, varies from 0.7–1.0 m in April to 1.0–1.6 m in July–September and decreases thereafter in the northwest (NW) and northeast (NE) sectors. This temporal variation of modal SIT agrees with the air temperature (correlation coefficients >0.5). The southwest (SW) sector shows a consistently low modal SIT (<1.0 m) because of the production of new ice in polynyas and continuous northward sea ice drift. Meanwhile, the southeast (SE) sector shows the thickest ice in Octobers 2019 and 2020 because of the advection of thick ice from the Amundsen Sea, which was reduced in 2021 and 2022. In terms of dynamic sea ice deformation, the SE sector shows the largest deformation because of the wind-driven convergence of sea ice movement. However, such intense deformation in the SE sector diminished in 2021 and 2022 due to the dominance of strong southerly wind associated with the Amundsen Sea Low (ASL). This study emphasizes the potential of IS2 sea ice products to assess the role of atmospheric driving forces on thermodynamic and dynamic sea ice changes.

Plain Language Summary The movement of sea ice is primarily driven by wind speed and direction. Furthermore, wind changes sea ice surface topography by forming sea ice deformation features. When sea ice floes collide with each other, the piled-up sea ice fragments form thicker ice, namely, pressure ridges. Observation of such pressure ridges in the Southern Ocean has been limited to specific seasons or regions because of the lack of high-resolution remote sensing data. However, high-resolution observation of pressure ridges is now available regularly through NASA's satellite altimeter ICESat-2. We investigate the spatiotemporal variations of sea ice topography in the Ross Sea, especially the distribution of pressure ridges, by using ICESat-2 data. The observation from ICESat-2 shows that the areal fraction of pressure ridges in the Ross Sea decreased in 2021 and 2022, particularly in the southeast Ross Sea. The comparison with weather data indicates that this decrease might be caused by strong southerly winds associated with the deep Amundsen Sea Low in these 2 years. This study demonstrates that ICESat-2 can play an important role in understanding the influence of wind on sea ice drift and the formation of pressure ridges.

1. Introduction

Antarctic sea ice plays an important role in the regional and global climate in the aspects of albedo feedback (Dickinson et al., 1987; Riihelä et al., 2021), deep water formation (Ohshima et al., 2013, 2016; Toggweiler & Samuels, 1995), ocean and atmospheric circulation (Cavalieri & Parkinson, 1981; England et al., 2020; Marzocchi & Jansen, 2017), and also in polar ecology (Massom & Stammerjohn, 2010; Stammerjohn et al., 2008). While the Antarctic sea ice extent slightly increased from 1979 to 2014 (Parkinson, 2019; Parkinson & Cavalieri, 2012), it started to decrease thereafter and has recorded historic minima in the summers of 2022, 2023, and 2024 in a row (Gilbert & Holmes, 2024; Liu et al., 2023; Raphael & Handcock, 2022; Turner et al., 2022; Wang et al., 2022). Furthermore, following the summer sea ice minimum in 2023, the autumn and winter sea ice extent also recorded the all-time minima in the Southern Ocean (Gilbert & Holmes, 2024; Purich & Doddridge, 2023). Such a rapid sea ice loss in the Southern Ocean might be associated with various thermodynamic and dynamic
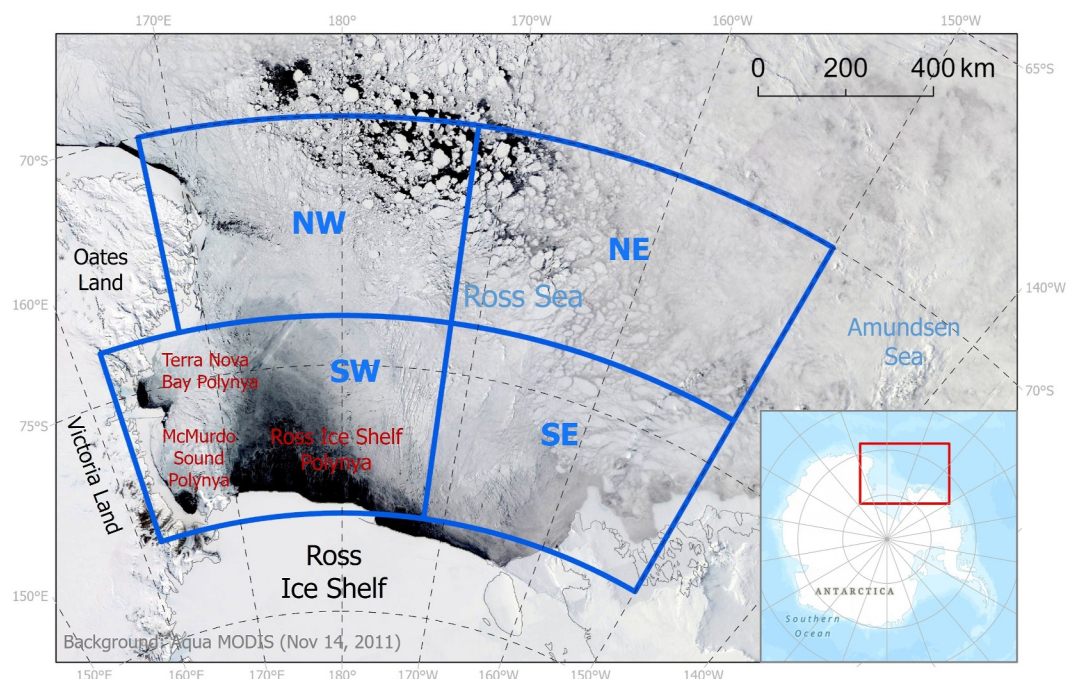
Figure 1. The defined four sectors (northwest–NW, southwest–SW, northeast–NE, and southeast–SE) of Ross Sea and locations of three large polynyas (dark area showing open water): Ross Ice Shelf polynya (RISP), McMurdo Sound polynya (MSP), and Terra Nova Bay polynya (TNBP), all sitting in the SW sector. Satellite true color imagery was acquired by Aqua MODIS on 14 November 2011.

interactions between the atmosphere and ocean, including positive Southern Annular Mode (SAM), La Niña events, and warming ocean temperature (Liu et al., 2023; Purich & Doddridge, 2023; Wang et al., 2022). Among several regions of the Southern Ocean, the Ross Sea contributed significantly to this loss trend, accounting for approximately 46% of the total circumpolar loss, due to greater sea ice transport triggered by the deepening of the Amundsen Sea Low (ASL) and resultant ocean warming (Turner et al., 2022). Thus, understanding the thermodynamic and dynamic sea ice mechanisms in the Ross Sea and their impact on the Southern Ocean and global climate systems is of great significance.

The sea ice conditions in the Ross Sea primarily result from persistent offshore wind blowing from the land. In particular, the coastal latent heat polynyas, formed by strong katabatic winds, play an important role in the formation, advection, and deformation of sea ice in the Ross Sea (Dale et al., 2017). There are three recurring large polynyas in the Ross Sea: Ross Ice Shelf polynya (RISP), McMurdo Sound polynya (MSP), and Terra Nova Bay polynya (TNBP) (Kwok et al., 2007; Tamura et al., 2008) (Figure 1). The RISP and MSP tend to occur simultaneously because they are caused by strong Ross Air Stream (RAS) events from the Ross Ice Shelf (Coggins et al., 2014). The TNBP is also a result of strong katabatic winds blown from the East Antarctic plateau channeled through the valleys of the Transantarctic Mountains (Van Woert, 1999).

While new and young ice is actively formed in these polynyas, dynamic ice deformation also occurs when ice is pushed away from polynyas, primarily eastward from the TNBP and northward from the RISP and MSP, due to compressional forces exerted by the katabatic winds against the pre-existing pack ice. As a result, deformation structures of packed ice, such as rafting and ridging, are often observed at the edge of the polynya ice regime (Hollands & Dierking, 2016). For example, Rack et al. (2021) investigated the sea ice thickness (SIT) distribution around the Terra Nova Bay and McMurdo Sound polynyas using airborne electromagnetic induction measurements in November, at the end of the spring growth season. They found that ~80% of the sea ice volume is heavily deformed and SIT in this region is thicker than the central Ross Sea, with pressure ridges of 3.0–11.8 m thickness.

Beyond the boundary of the Ross Sea, many studies have also noted that Antarctic sea ice is substantially deformed. According to 3D floe-scales maps of sea ice draft retrieved from autonomous underwater vehicles (AUV), an average 57% of the sea ice area and 76% of the total ice mass are deformed in the Weddell,

Bellingshausen, and Wilkes Land sectors of Antarctica (Williams et al., 2015). Williams et al. (2015) suggested that the major mechanism of thickening or deformation might be the breakup of ice floes through repeated collisions or shear events and subsequent consolidation into rubble fields. Tin and Jeffries (2003) used drill profile data to identify the morphology of sea ice deformation features in various regions of the Southern Ocean, including the Ross, Amundsen, Bellingshausen, and Weddell Seas. They categorized the deformed sea ice features into three shapes: coupled ridges, widowed ridges, and rubble piles. They found that coupled ridges, widowed ridges, and rubble piles have 27, 15, and 43 m of mean keel width and 2.41, 1.40, and 1.12 m of mean keel depth, respectively. Worby et al. (1996) investigated ice thickness and deformation of sea ice in the Bellingshausen and Amundsen Seas using in situ and ship-based measurement data. Their result showed that ridge sails typically have 0.3–0.6 m thickness, and approximately 25% of the pack ice is deformed.

Nevertheless, these studies were restricted to a specific location or time because of the limited availability of high-resolution SIT data. Given that harsh weather and long polar nights limit the chance of regular in situ or airborne campaigns, spaceborne remote sensing can be the most efficient way to regularly monitor SIT in the Southern Ocean. In general, satellite altimeters measure sea ice freeboard, the height of sea ice surface above local sea level, by distinguishing signals from sea ice and open water lead surfaces. Then, this freeboard is converted to SIT by using (a) the hydrostatic equation with snow depth and the densities of ice, water, and snow and/or (b) empirical equations (Ozsoy-Cicek et al., 2013; Xie et al., 2011, 2013). Although satellite altimeters have estimated SIT over the Southern Ocean at regular intervals (Kern et al., 2016; Kwok, 2010; Li et al., 2018), observation of detailed sea ice topography via satellite altimeters is challenging because it requires higher spatial resolution and precision. Particularly, most of the previous spaceborne altimeters do not have enough precision or resolution to resolve tens-of-meter ridges: for example, the ICESat laser altimeter (2003–2009) had a 70 m diameter footprint and 170 m spacings (Zwally et al., 2002), and the CryoSat-2 radar altimeter, operated since 2010, has a 300 m along-track by 1.5 km across-track footprint (Wingham et al., 2006). However, recently, ICESat-2 (IS2) has been able to detect sea ice surface topography with unprecedented precision and resolution using a state-of-the-art photon counting system called Advanced Topographic Laser Altimeter System (ATLAS) (Markus et al., 2017). IS2 ATLAS transmits laser pulses of 532 nm wavelength at 10 kHz and detects the traveling time of individual photons reflected back from the surface (Neumann et al., 2019). When these laser pulses reach the earth's surface from the IS2 nominal orbit altitude ($\sim$500 km), the laser footprints are $\sim$11 m diameter separated by $\sim$0.7 m along ground tracks (Magruder et al., 2020; Neumann et al., 2019).

The fine resolution of IS2 ATLAS opens a new opportunity to measure regional patterns of sea ice deformation over a large area at regular intervals. Ricker et al. (2023) assessed the capability of IS2 to capture sea ice surface topography and roughness using a helicopter-based airborne laser scanner (ALS). They found that the IS2 strong beams can detect up to 42% of pressure ridges and sails detected by the ALS data. Farrell et al. (2020) demonstrated that IS2 can capture surface roughness, ridge height, ridge frequency, melt pond depth, floe size distribution, and lead frequency with vertical height precision of 0.01 m. Additionally, Duncan and Farrell (2022) investigated the characteristics and distribution of pressure ridges (e.g., frequency of ridges, height of ridges, surface roughness, and ridging intensity) in Arctic sea ice using the IS2 data. Koo, Lei, et al. (2021) also showed that the IS2 ATL10 product can explain the thermodynamic and dynamic sea ice growth efficiently as compared with sea ice mass balance array (SIMBA) buoy data. However, these previous studies have concentrated on the Arctic sea ice; the spatiotemporal distributions of pressure ridges in the Ross Sea and other areas of the Southern Ocean have not been previously investigated using IS2 data.

Therefore, by leveraging the capability of the IS2 sea ice product to detect detailed sea ice surface topography, this study examines the spatiotemporal variations of sea ice deformation in the Ross Sea. Interpretation of these sea ice deformation features provides an important clue to understanding thermodynamic and dynamic ice processes in the Ross Sea. Based on the findings from the IS2 sea ice measurements, we also explore what environmental variables affect the dynamic sea ice changes. Considering the Ross Sea is dominated by strong katabatic winds blowing from the Ross Ice Shelf or from the East Antarctic plateau, we focus on how the katabatic winds and the resultant presence of polynyas lead to the dynamic deformation of sea ice around the polynyas.

2. Materials and Methods

2.1. ICESat-2 ATL10 Freeboard Product

We use IS2 Level 3A ATL10 sea ice product version 6 (Kwok et al., 2023) to extract sea ice topographical information in the Ross Sea from 2019 to 2022. The ATL10 product provides along-track freeboard measurement for six multiple beams (3 pairs of strong/weak beams) with approximately 2 cm of height precision (Kwok, Kacimi, et al., 2019). The ATL10 product is derived from the ATL07 sea ice surface height product, which is generated by aggregating 150 signal photons into a single height segment. The surface height of each ATL07 height segment is determined by fitting a Gaussian height distribution of these 150 signal photons. The length of the ATL07 height segment ranges from 10 to 200 m, on average 12–15 m (Kwok, Markus, et al., 2019). The mean height of the fitted histogram becomes the mean surface height of the height segment, and this surface height is referenced to the WGS84 ellipsoid. In addition to the surface height, the ATL07 product also classifies the surface types of each height segment into sea ice, dark lead, or specular lead (Kwok et al., 2021). The ATL10 product calculates the local sea reference height (h_{ref}) for every 10 km based on the specular leads from the ATL07 product. Once the sea reference height is derived, the sea ice freeboard (h_f) can be calculated by subtracting h_{ref} from the surface heights of sea ice (h_{obs}).

$$h_f = h_{obs} - h_{ref} \tag{1}$$

Herein, it should be noted that the sea ice freeboard measured by ATL10 represents the total freeboard (i.e., ice freeboard plus snow depth if there is snow on sea ice; the height of the air-snow interface above the local sea level reference) because the laser photons of 532 nm wavelength from IS2 do not substantially penetrate the snow layer. The ATL10 freeboard is available only where the daily sea ice concentration (SIC) is greater than 50% and at least 25 km away from the coast (Kwok et al., 2021). More details about the ATL10 product can be found in Kwok, Markus, et al. (2019) and Kwok et al. (2021).

2.2. Extraction of Thermodynamic and Dynamic Sea Ice Features From IS2

If repeated measurements within an ice floe are available, the temporal variation of the modal ice thickness (i.e., the thickness of level ice) around this floe can be considered as an indicator of thermodynamic ice growth (Koo, Lei, et al., 2021). We first extract the modal freeboard by applying a 3-km mode sampling to the IS2 ATL10 freeboard product (Figure 2). The modal freeboard is defined as the freeboard of the maximum density in the freeboard density distribution every 3 km (Figure 2). If a group of freeboard measurements $h_{f,n}(n = 1, 2, …,N)$ is given, the Gaussian kernel density at a certain freeboard value h_f ($\rho_K(h_f)$) is calculated by the following equation (Emanuel, 1962):

$$\rho_K(h_f) = \sum_{n=1}^{N} K(h_f - h_{f,n}; \alpha)$$

$$\text{where } K(x; \alpha) = \exp\left(-\frac{x^2}{2\alpha^2}\right) \tag{2}$$

where α is the bandwidth or smoothing parameter that controls the tradeoff between bias and variance in the result. This α value is set to be 0.1 m in this study. In the freeboard distributions for every 3 km along-track segment, the freeboard value at the maximum $\rho_K(h_f)$ is determined as the modal freeboard for this 3 km segment. After testing several segment lengths, we determine 3 km is the optimal distance to represent a statistically significant modal freeboard. Since the modal freeboard can vary across a regional scale, a too-long segment length can bring unnecessary biases to the modal freeboard and the identification of pressure ridges. On the other hand, if the segment length is too short, the modal freeboard can be biased to local ridges or leads. The 3-km modal freeboard values are assigned to individual IS2 ATL10 data points; the ATL10 data points grouped as the same 3-km segment have the same modal freeboard values (Figure 2).

Once the modal freeboard is determined, we convert the modal freeboard (h_f) into modal SIT (h_i) using the hydrostatic equation:
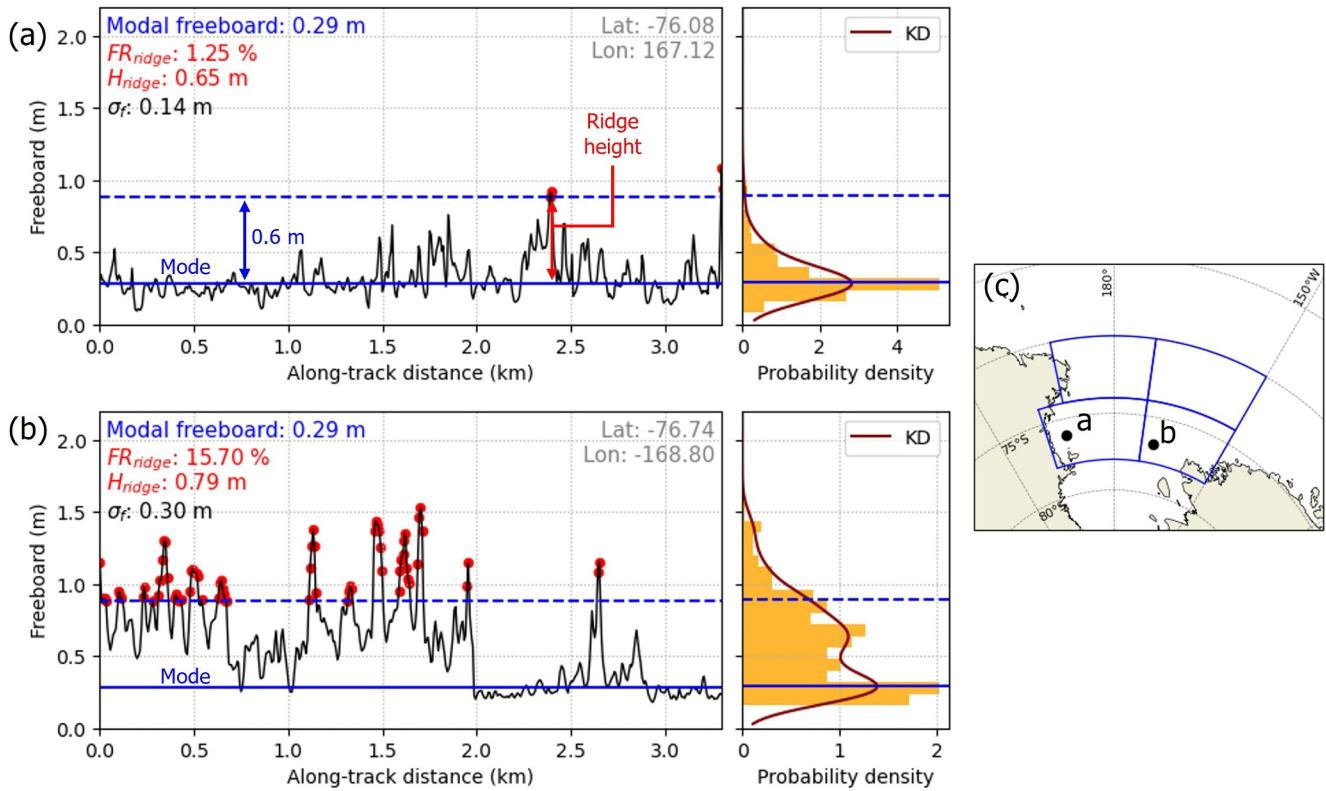
Figure 2. Freeboard profiles and histograms of two example 3-km segments on 20 October 2020: (a) is from the SW sector, and (b) is from the SE sector. The left panels of (a) and (b) show the freeboard profiles (solid black lines), local modal freeboard (solid blue lines), threshold for ridge detection (modal freeboard +0.6 m; dashed blue lines), and detected pressure ridges (red dots). The right panels of (a, b) show the Gaussian kernel density (KD) of the freeboard distributions. (c) Locations of (a, b) segments in the Ross Sea.

$$h_i = \left(\frac{\rho_w}{\rho_w - \rho_i}\right) h_f + \left(\frac{\rho_s - \rho_w}{\rho_w - \rho_i}\right) h_s \qquad (3)$$

where ρ_w, ρ_i, and ρ_s denote densities of water, ice, and snow, respectively; h_s denotes snow depth. In this study, ρ_w, ρ_i, and ρ_s are assumed to be 1,024, 917, and 340 kg/m^3 based on previous studies that derived Antarctic SIT from spaceborne freeboard measurements (Kacimi & Kwok, 2020; Kurtz & Markus, 2012; Xie et al., 2013; Xu et al., 2021). Regarding snow depth, some studies have calculated snow depth from total freeboard using their linear relationships (Kacimi & Kwok, 2020; Kurtz & Markus, 2012; Ozsoy-Cicek et al., 2013; Xie et al., 2013; Xu et al., 2021). Thus, taking this assumption, we calculate snow depth from the IS2 freeboard using the following linear equation proposed by Kacimi and Kwok (2020):

$$h_s = a h_f + b \qquad (4)$$

where a and b are the regression slope and intercept. Kacimi and Kwok (2020) suggested the best regression slope and intercept for each month from April to November based on the snow depth retrieved from IS2 and CryoSat-2; the slopes vary between 0.66 and 0.70, and the intercepts vary between −4.5 and −3.4 cm. For July, when the slopes and intercepts are not available due to data unavailability, we use the slope and intercept for June. We also use the slope and intercept of November for the December snow depth. The retrieved modal SIT is mapped on the 25-km grid of the National Snow and Ice Data Center (NSIDC) sea ice south polar stereographic projection by assigning the average of the modal SIT from all data points within a grid cell (to the grid cell).

Besides the modal SIT, three dynamic features are also calculated on the 25-km grid of the NSIDC sea ice south polar stereographic projection: ridge fraction (FR$_{ridge}$), mean ridge height (H_{ridge}), and surface roughness (σ_f)

Table 1
Thermodynamic and Dynamic Sea Ice Features Derived From IS2 Data

Features	Method
Modal sea ice thickness (SIT)	Sea ice thickness at the maximum kernel density for every 3-km along-track distance; the average from all ATL10 data points within a 25 km grid cell is assigned to each grid cell
Ridge fraction (FR_{ridge})	Fractional length of all ridge points (>0.6 m freeboard above the 3-km modal freeboard); calculated from all ATL10 data points within a 25 km grid cell
Mean ridge height (H_{ridge})	Mean height of all ridge points above the level ice surface; calculated from all ridge points within a 25 km grid cell
Surface roughness (σ_f)	Standard deviation of freeboard for every 3-km along-track distance; the average from all ATL10 data points within a 25 km grid cell is assigned to each grid cell

(Table 1). First, pressure ridges can be captured as the parts with freeboard higher than 0.6 m above the level sea ice (Duncan & Farrell, 2022; Duncan et al., 2020; Farrell et al., 2020; Koo, Lei, et al., 2021). If the freeboards of ATL10 data points are greater than the modal freeboard +0.6 m, we determine those data points as pressure ridges (Figure 2). Once all pressure ridges are identified, the ridge fraction (FR_{ridge}) on a 25 km grid cell is calculated by the following equation:

$$FR_{ridge} = \frac{L_{ridge}}{L_{total}} \times 100 \ (\%) \tag{5}$$

where L_{ridge} is the summed length of all ridges within the 25 km grid cell, and L_{total} is the total effective length of IS2 track within the 25 km grid cell. Additionally, the mean ridge height H_{ridge} is calculated as the mean height of the detected ridges above the level ice surface within a 25 km grid cell. The standard deviation of freeboard (σ_f), as a proxy of surface roughness, is calculated for all data points every 3 km along-track distance, and the average of σ_f from all data points within a grid cell is assigned to that grid cell.

By using this 25-km gridded product, we extract the monthly variations of these four features in four different regions of the Ross Sea (i.e., northwest, northeast, southwest, southeast) (Figure 1). Since the fidelity of IS2 freeboard measurements can deteriorate in summer months of low SIC from January to March, we conduct the temporal analysis for only April to December of each year.

2.3. Comparison With ERA-5 Reanalysis Data

The objective of this study is to characterize how the thermodynamic and dynamic sea ice features have changed and what environmental factors have contributed to such changes. Thus, in order to correlate the variations of sea ice features with the atmosphere and ocean interactions, we use meteorological data from the ERA5 global reanalysis (Bell et al., 2021; Hersbach et al., 2020). As a reanalysis replacement of the ERA-Interim reanalysis, ERA5 reanalysis provides a number of atmospheric, ocean-wave, and land-surface quantities for the last 80 years from 1940 onwards. ERA5 is produced using 4D-Var data assimilation and model forecasts in CY41R2 of the ECMWF (European Center for Medium-Range Weather Forecasts) Integrated Forecast System (IFS). We obtain hourly and monthly air temperature, wind velocity, mean sea level pressure, and SIC data in the Ross Sea from 2019 to 2022 with 0.5° × 0.5° spatial resolution. Then, we reproject these data into the 25-km grid of the NSIDC sea ice south polar stereographic projection and qualitatively compare them with the temporal patterns of the thermodynamic and dynamic features.

3. Results

3.1. Spatiotemporal Variations of Modal Ice Thickness

Figure 3 shows the monthly variations of the modal SIT for each sector from 2019 to 2022. Considering the modal SIT indicates the level sea ice surface, the spatiotemporal changes of the modal thickness can be caused by two processes: (a) thermodynamic ice growth and (b) advection of sea ice from a different location. The SW sector shows the lowest modal SIT (<1.0 m) for all seasons, and this sector shows that the SIT increase was less than 0.2 m during the freezing season (April to September). The continuously low SIT in this sector is attributed to (a)
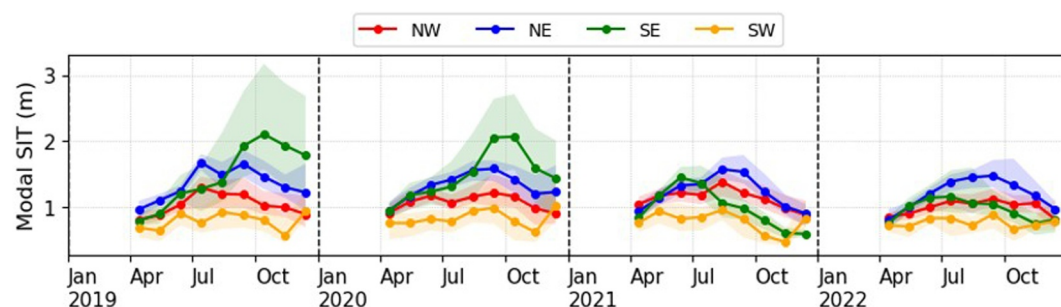
Figure 3. Monthly variations of modal sea ice thickness for each sector from 2019 to 2022. The solid lines indicate the regional averages, and the colored areas indicate the ranges between 25% and 75% quantiles. The vertical dashed lines indicate the first day of the year.

production of new ice in the recurring polynyas and (b) continuous northward sea ice drift. As shown in Figure 4, a large polynya (i.e., RISP) of thin ice (<0.5 m of SIT) is observed in the SW sector in all seasons. Since the katabatic wind pushes sea ice away to the north and new ice is continually formed on the polynya, the overall SIT in this sector remains low compared to the other sectors.

Next, the modal SIT in the NW sector varies from 0.7–1.0 m in April to 1.2–1.4 m in July to September and decreases again thereafter, and this behavior has no significant interannual variability. This sector shows the second lowest SIT increase among the four sectors, which is associated with the influence of thin ice advected from the SW sector and piled up in the NW sector. In the NW sector, for the most part, the modal SIT increases gradually from south to north because sea ice is pushed away and first piled up on the edges of the RISP polynya (Figure 4). Near the coast north of the TNBP and MSP polynyas, thick ice is also seen (Figure 4), in agreement with Rack et al. (2021), who observed very thick ice caused by continued deformation as the ice was advected
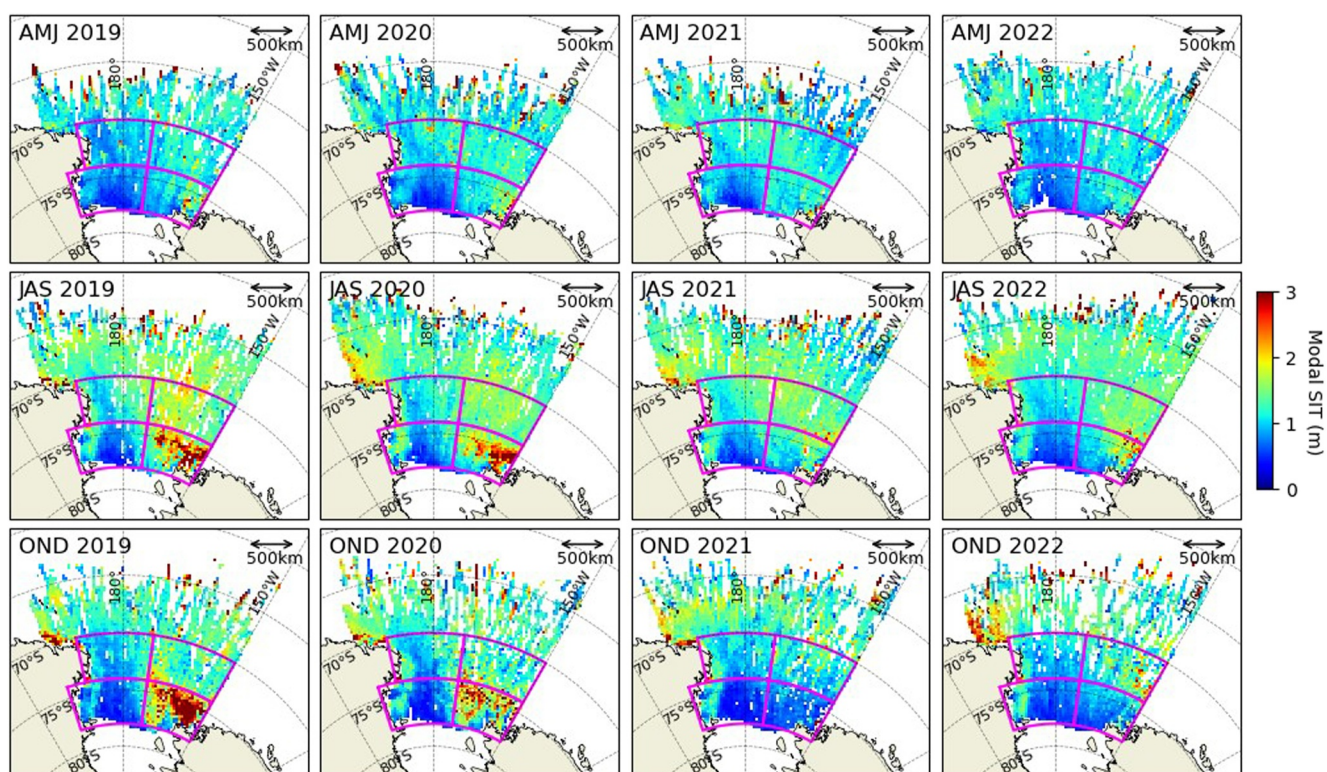

Figure 4. Maps of the modal sea ice thickness for 3 month periods from April to December: April–May–June (AMJ), July–August –September (JAS), and October–November–December (OND) in the Ross Sea from 2019 to 2022. The magenta lines indicate the boundary of each sector.
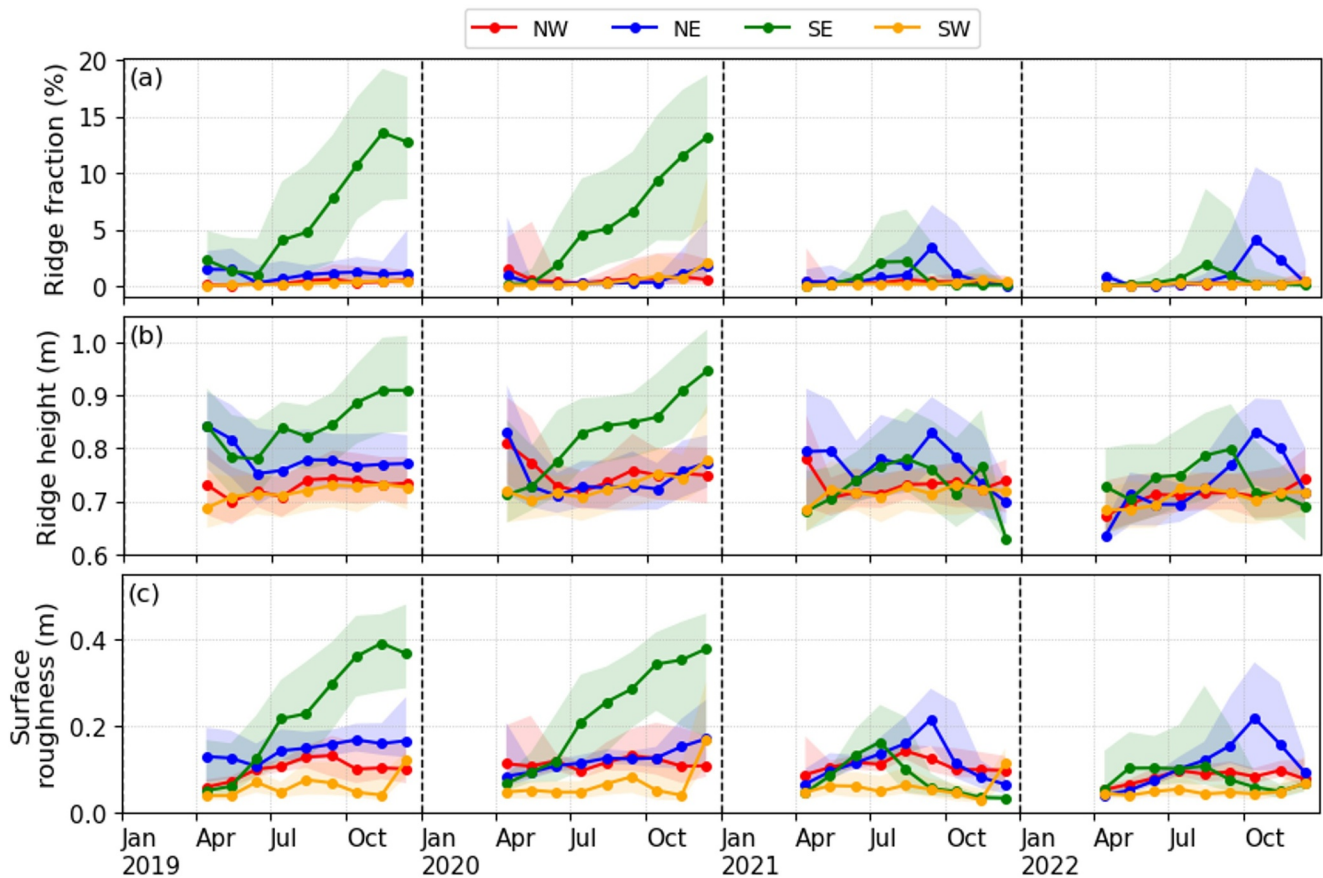
Figure 5. Monthly variations of (a) ridge fraction, (b) mean ridge height, and (c) surface roughness for each sector from 2019 to 2022. The solid lines indicate the regional averages, and the colored areas indicate the ranges between 25% and 75% quantiles. The vertical dashed lines indicate the first day of each year.

northward. The thin ice in the NW sector continues drifting northward, piling up and thickening beyond the NW sector (clearly seen in Figure 4). The temporal variations of modal SIT in the NE sector appear similar to the NW, but the NE sector shows overall thicker ice. The modal SIT in this sector is 0.8–1.0 m in April, reaches up to 1.4–1.7 in winter months from July to September, and then reduces to 1.0–1.2 m in December. This behavior appears somehow consistent during the period of 2019–2022.

Finally, the SE sector shows the largest intra-annual and inter-annual variability among the four sectors. In 2019 and 2020, the SE sector showed the greatest increase in modal SIT from 0.7–1.0 m in April to 2.0 m in October (Figure 3). When the SE sector is compared to the other sectors, the most interesting feature is that the peak of modal SIT is observed in October, whereas the peak of modal SIT is observed from July to September for the other sectors. The 2–3 months delay of the SIT peak in the SE sector might be attributed to the inflow of thick ice from the Amundsen Sea (DeLiberty et al., 2011; Koo, Xie, et al., 2021). However, 2021 and 2022 show completely different behavior from the previous 2 years. In 2021 and 2022, the thickest ice occurred from June to July, only reaching 1.2–1.5 m, and then SIT decreased gradually until December.

3.2. Spatiotemporal Variations of Dynamic Features

In addition to the modal SIT, we investigate the temporal variations of three dynamic features (i.e., ridge fraction, mean ridge height, and surface roughness) for each sector (Figure 5). First, in terms of ridge fraction (Figures 5a and 6), it is notable that 2021 and 2022 show different behaviors from 2019 to 2020. In 2019 and 2020, the ridge fraction of the SE sector reached a maximum greater than 10% in November–December. However, in 2021 and 2022, the ridge fraction in the SE sector dramatically decreased to less than 3%, and the period of maximum ridge fraction is almost 3 months ahead (July to August). Furthermore, in 2021 and 2022, the NE sector shows even greater ridge fractions than the SE sector in September to October. The northward transition of high-ridge-fraction
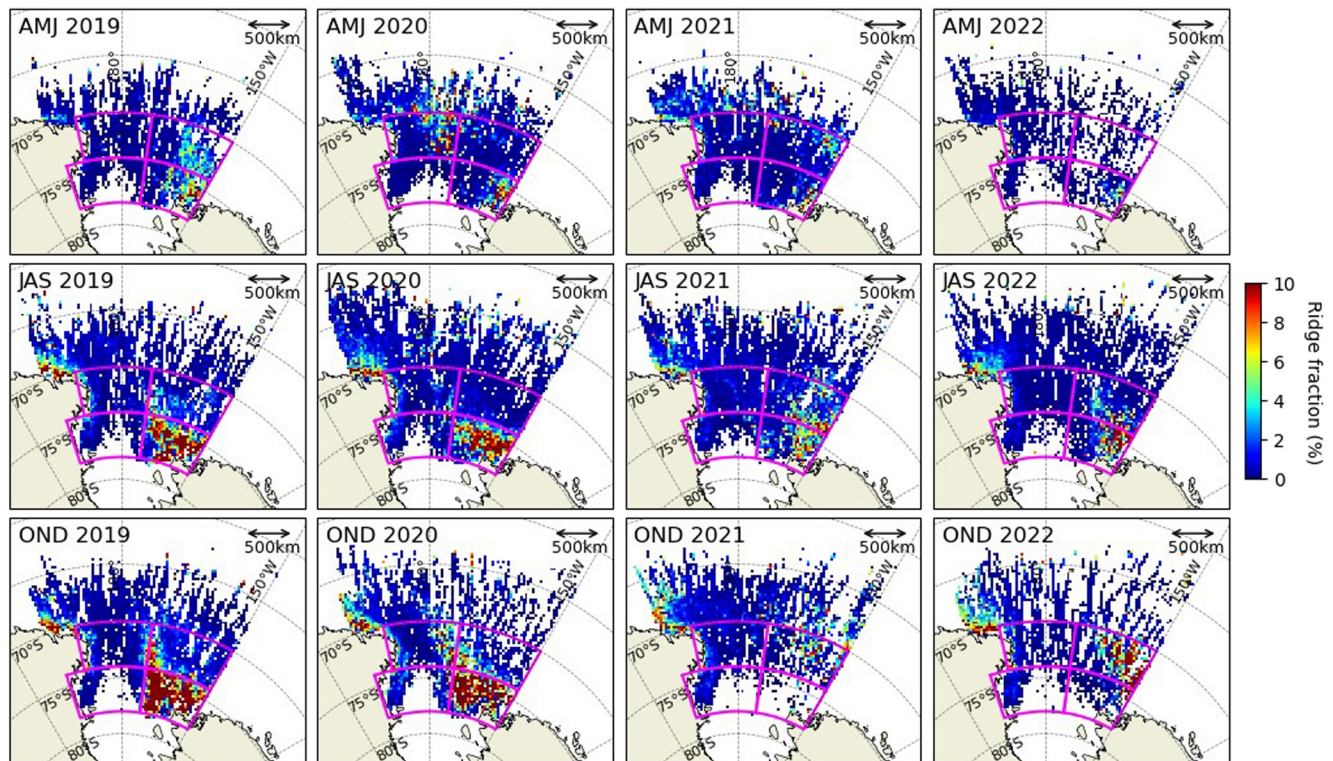
Figure 6. Maps of the ridge fraction for 3 month periods from April to December: April–May–June (AMJ), July–August–September (JAS), and October–November–December (OND) in the Ross Sea from 2019 to 2022. The magenta lines indicate the boundary of each sector.

regions from 2019–2020 to 2021–2022 can also be found in Figure 6. In contrast with the NE and SE sectors, the NW and SW sectors remain nearly 0%–1% of ridge fractions due to newly formed thin ice in the coastal polynyas.

The spatiotemporal variations of ridge height (Figures 5b and 7) and surface roughness (Figures 5c and 8) appear similar to that of ridge fraction (Figures 5a and 6). The SE sector shows the greatest ridge height (>0.9 m) and surface roughness (0.35–0.40 m) in November–December of 2019–2020 because of the inflow of thick ice from the Amundsen Sea (Figure 9 and Figure S3 in Supporting Information S1), but they decreased to <0.8 m and <0.2 m, respectively, in 2021–2022. Instead, the NE sector shows a significant increase in ridge height and surface roughness in 2021–2022, leading to ridge heights greater than 0.8 m and surface roughness greater than 0.2 m in September to October. The SW and NW sectors show slightly increasing or consistent ridge heights and surface roughness all over the months from 2019 to 2022 due to the newly formed thin ice around polynyas. Similar to the ridge fraction, the regions of higher ridge heights and roughest surfaces in the SE sector in 2019–2020 move toward the NE sector in 2021–2022 (Figures 7 and 8).

4. Discussion

4.1. Linkage to Weather Data

We compare thermodynamic and dynamic sea ice features with the temporal variations of weather data from ERA5 reanalysis to examine how atmospheric conditions affect the thermodynamic and dynamic behaviors of sea ice. Monthly average air temperature, SIC, u-component wind (eastward wind velocity), and v-component wind (northward wind velocity) from ERA5 reanalysis data are depicted in Figure 10. In terms of temperature, the southern sectors (SE and SW) show relatively lower temperatures than the northern sectors (NE and NW). The minimum temperature is generally recorded from June to August, though the exact minimum month varies by year. After the winter season, air temperature increases rapidly in September and reaches almost 0°C from December to February. Such temperature variations agree well with the temporal variations in the modal SIT in the NW and NE sectors (Figure 3). In the NW and NE sectors, the sharp increase of the modal SIT from April to July corresponds to the rapid thermodynamic ice growth due to the drop in air temperature during these months.
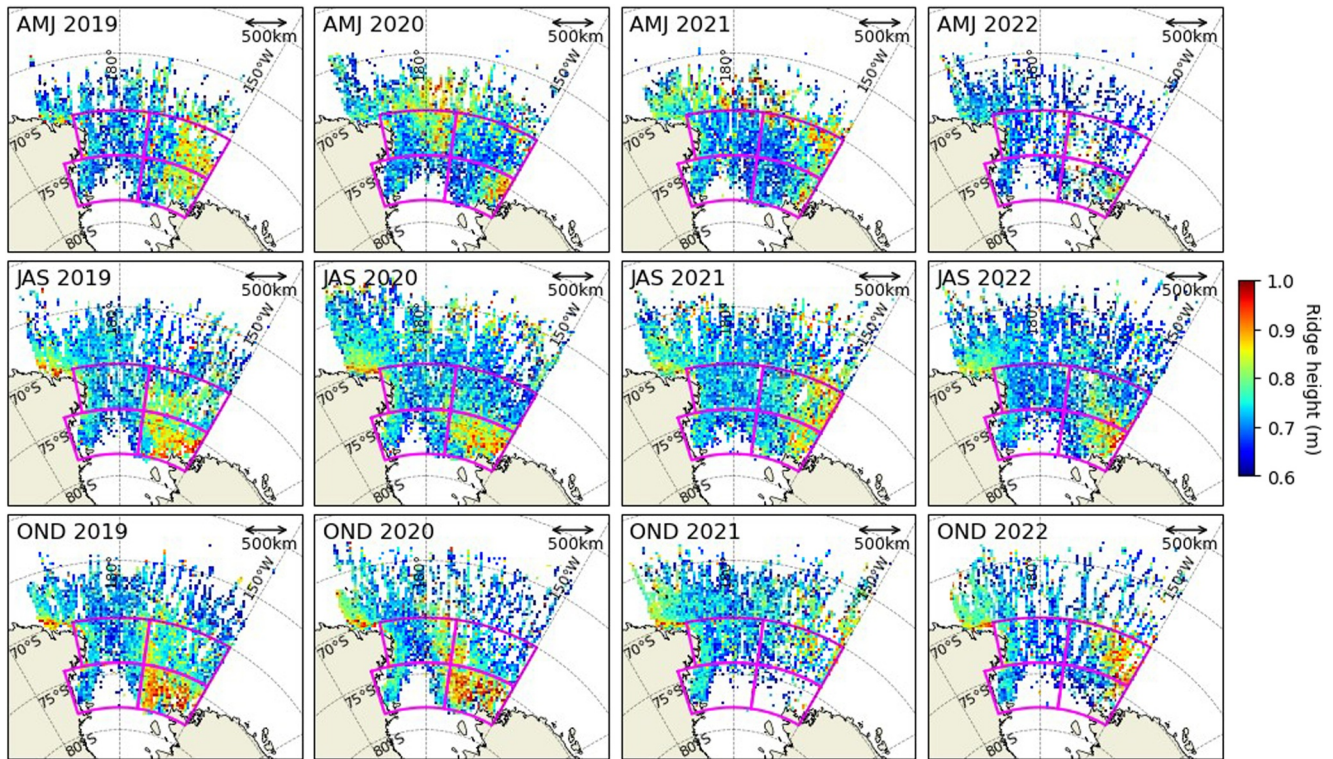
Figure 7. Maps of the mean ridge height for 3 month periods from April to December: April–May–June (AMJ), July–August–September (JAS), and October–November–December (OND) in the Ross Sea from 2019 to 2022. The magenta lines indicate the boundary of each sector.
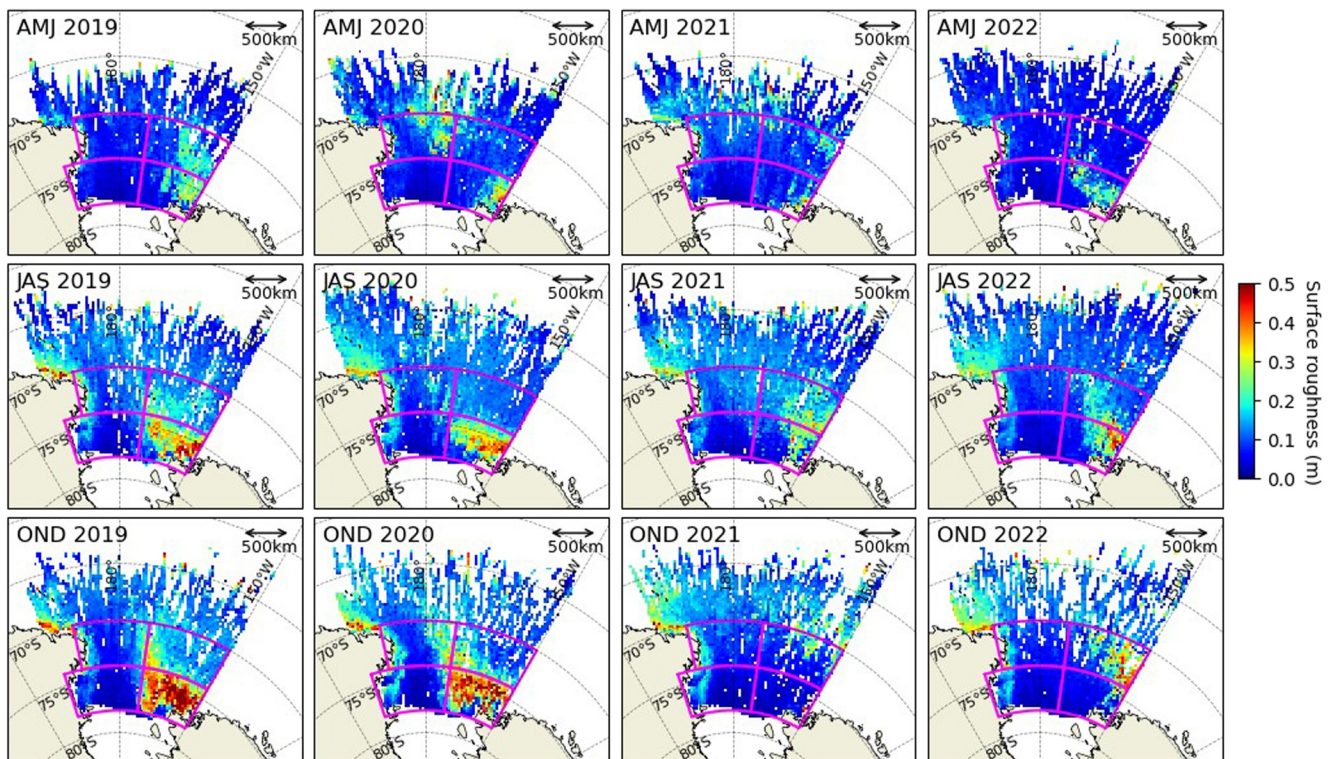

Figure 8. Maps of the surface roughness for 3 month periods from April to December: April–May–June (AMJ), July–August–September (JAS), and October–November–December (OND) in the Ross Sea from 2019 to 2022. The magenta lines indicate the boundary of each sector.
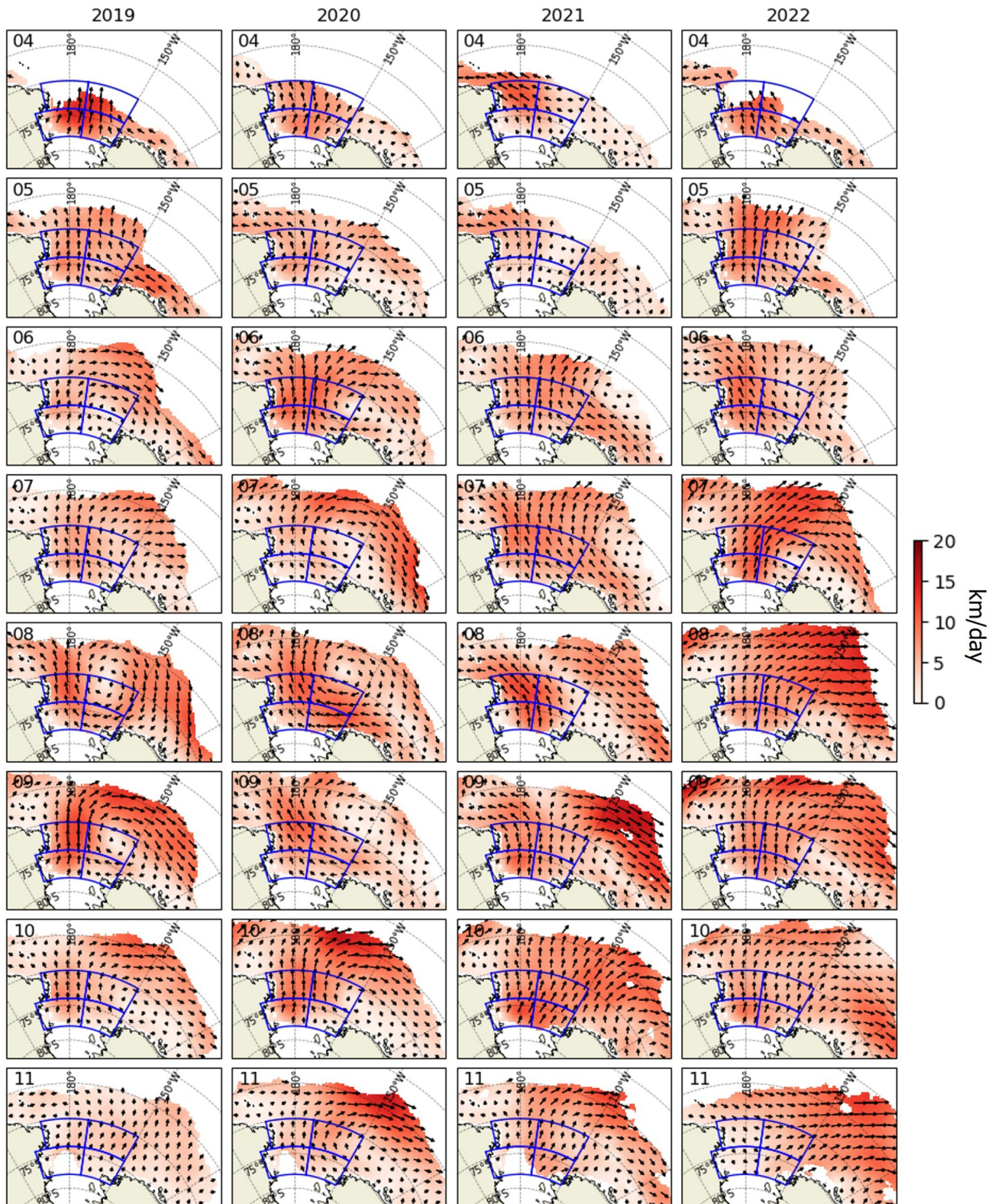
Figure 9. Monthly sea ice drift in the Ross Sea and Amundsen Sea in April–November from 2019 to 2022. The four sectors in the Ross Sea are indicated as blue boxes. Sea ice drift is acquired from the NSIDC polar pathfinder daily sea ice motion vector data (Tschudi et al., 2019). It is noted that the sea ice drift pattern has changed in the SE sector comparing 2019–2020 and 2021–2022.
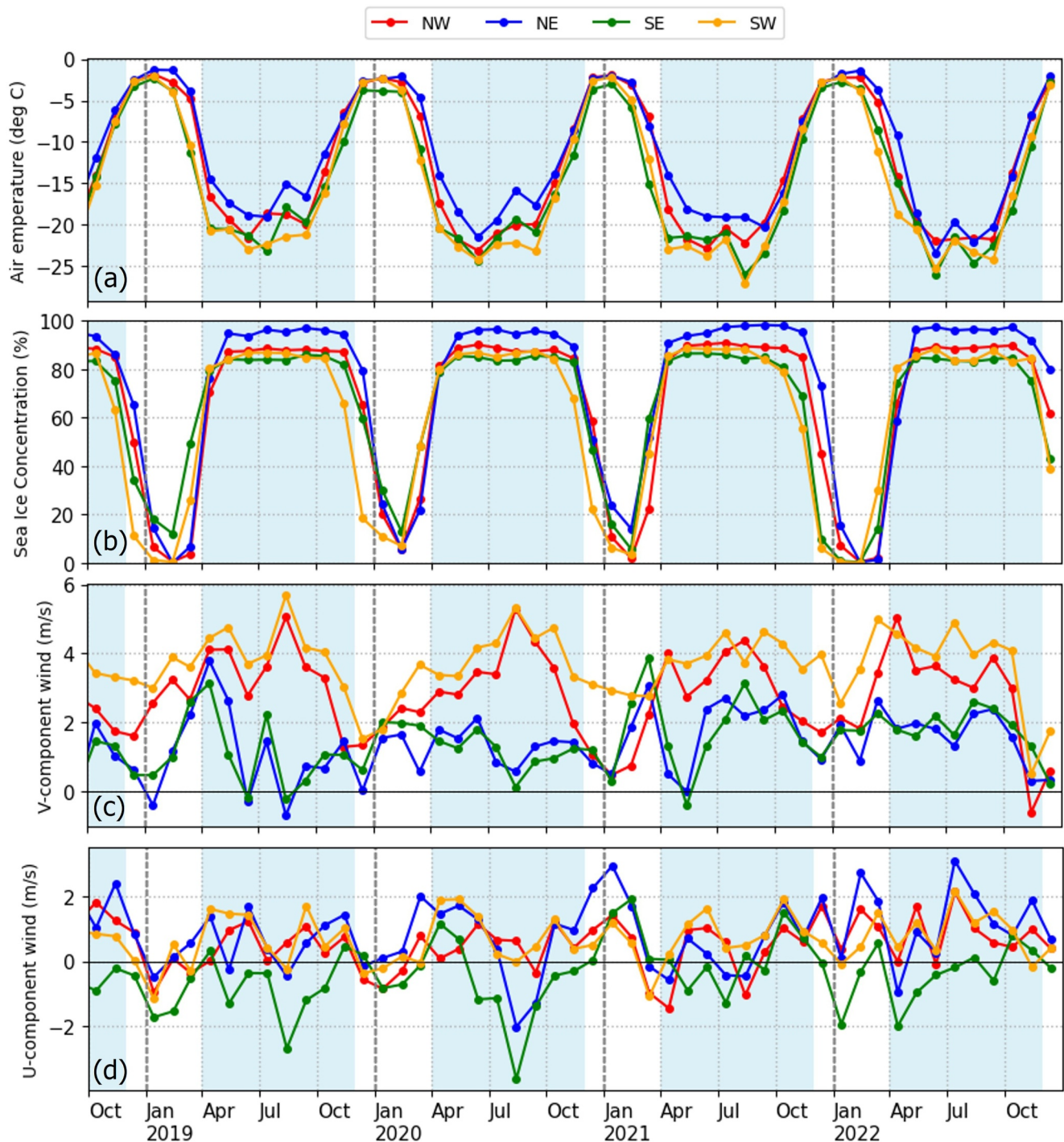
Figure 10. Monthly (a) air temperature, (b) sea ice concentration (SIC), (c) v-component wind velocity (northward), and (d) u-component wind velocity (eastward) from October 2018 to December 2022. The blue shaded areas indicate April to November when SIC >50%. A positive v-component wind means northward (southerly) wind, and a negative v-component wind means a southward (northerly) wind. A positive u-component wind means eastward (westerly) wind, and a negative u-component wind means westward (easterly) wind.

Additionally, after the modal SIT records the maximum in July–September, it starts to decrease along with the warming temperature. The Pearson's correlation coefficients between the modal SIT and air temperature are 0.57 (p-value = 0.004) and 0.81 (p-value <0.001) for the NW and NE sectors, respectively, implying that
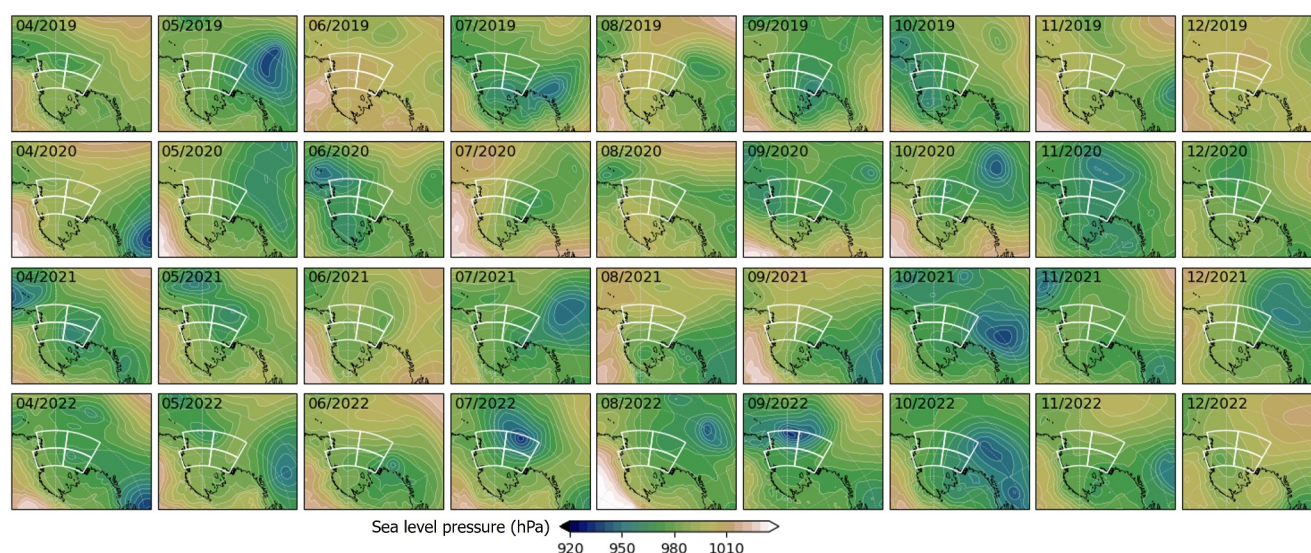
Figure 11. Mean sea level pressure near the Ross Sea and Amundsen Sea from 2019 to 2022. Deep Amundsen Sea Low is clearly seen in Octobers of 2021 and 2022.

thermodynamic ice freezing and melting accounts for significant SIT changes in these regions (see Figure S4 in Supporting Information S1 for more details).

However, in the case of the SE, substantial offsets are found between the minimum temperature months and maximum modal SIT months. In 2019 and 2020, the modal SIT recorded the maximum in October. If the variations of the modal freeboard of the SE sector were purely driven by thermodynamic ice freezing and melting, this maximum modal freeboard should be in August/September, as seen for the NW and NE sectors. However, the delay of maximum modal freeboard in the SE sector shows that the SIT in this sector is significantly affected by the inflow of thick multi-year ice (MYI) ice from the Amundsen Sea (Figure 9 and Figure S3 in Supporting Information S1) (DeLiberty et al., 2011; Koo, Xie, et al., 2021), besides the thermodynamic processes. Additionally, the SW sector shows a consistently low modal SIT regardless of temperature variations, which is attributed to the strong northward sea ice advection (Figure 9) and continuous production of new ice in the large polynyas (Morales Maqueda et al., 2004; Nihashi & Ohshima, 2015; Tamura et al., 2008). Indeed, in these two southern sectors, Pearson's correlation coefficients between the modal SIT and air temperature are 0.46 (p-value = 0.023) and 0.49 (p-value = 0.017) for the SE and SW sectors, respectively, which are lower than those of NW and NE sectors. These lower correlations in the SE and SW sectors imply that the advection of sea ice contributes to the temporal variations of modal SIT in addition to pure thermodynamic ice freezing and melting.

The air temperature variations are also correlated with the SIC variations (Figures 10a and 10b). SIC records the minimum at almost zero in January–February, when the temperature is close to above the freezing point. Throughout April to October, SIC remains consistently at above 80%, and the NE sector shows the maximum SIC at 95%–100%. While the SIC of the SE sector in 2019 and 2020 remained consistent at above 80% until November, SIC in 2021 and 2022 started to decrease in October. Consequently, the SE sectors became nearly ice-free (SIC <10%) in December 2021, which was almost 2 months ahead compared to the previous years. The earlier and faster SIC reduction in the SE sector in 2021 and 2022 can be associated with the changes in wind directions and the resultant reduced inflow of sea ice from the Amundsen Sea in the spring of 2021 and 2022 (Figure 9). The transition in the atmospheric circulation was likely caused by the deep ASL in 2021 and 2022. As shown in Figure 11, while the ASL was not clearly observed in the springs of 2019 and 2020, a deep ASL was intensified in Octobers 2021 and 2022. The strong southerly wind moved sea ice away from the coast in the Ross Sea, eventually exposing the low albedo ocean to increased solar heating and accelerating the melting of sea ice in January and February 2022 (Turner et al., 2022).

As shown in Figure 10c, consistent and relatively strong southerly wind (>2 m/s) was observed in the SE and NE sectors in April–November of 2021/2022, while the southerly wind speed did not generally exceed ~2 m/s in April–November of 2019/2020. Since strong southerly wind pushes sea ice away from the SE sector in 2021/

2022, the thick ice from the Amundsen Sea cannot reach the Ross Sea or cannot remain there even after reaching the Ross Sea (i.e., moving quickly northward to the NE sector). On the other hand, as for the easterly wind, a strong westward wind blew in the SE sector in 2019/2020 (Figure 10d). While the other sectors show slight eastward wind, the SE sector alone shows westward wind velocity greater than ∼2 m/s (Figure 10d). This westward wind dragged thick ice from the Amundsen Sea into the SE sector of the Ross Sea in 2019 and 2020 (Figure 9 and Figure S3 in Supporting Information S1). Considering that the westward thick ice from the Amundsen Sea confronts northward coastal ice from the Ross Ice Shelf in the SE sector (Figure 9), it was likely that the convergent interaction between them caused the formation of pressure ridges. However, as this westward wind in the SE sector abated in 2021 and 2022, thick ice from the Amundsen Sea was not carried into the SE sector, reducing the chance of convergent sea ice deformation. Consequently, the transition of wind direction in 2021/2022 resulted in a low modal freeboard (Figure 3) and less chance of the active formation of pressure ridges (Figure 5) in the SE sector in these years.

4.2. Deformation Around Polynyas

Although we capture and compare general deformation patterns over the Ross Sea on a large scale (25 km grid map) and a monthly period, we also explore small-scale snapshots of deformation features around the polynyas using IS2 ATL10 freeboard measurements. As sea ice is pushed out by strong katabatic winds, sea ice on the edges of the polynyas is likely to be piled up and deformed. Thus, we obtain some snapshots of IS2 freeboard measurements around polynya events and check if IS2 captures such deformation events. First, we identify several occurrences of RISP in 2019–2022 by using Sentinel-1 (S1) synthetic aperture radar (SAR) images (Dai et al., 2020): polynyas can be characterized by white streaks in SAR images as shown in Figure 12. Then, we search for the IS2 ATL10 tracks coincident with these images and extract the freeboard profiles near the polynyas. Several examples of the freeboard profiles during polynya events are shown in Figure 12. Most interesting is that sharp or smooth peaks of freeboard are observed at the edges of the polynya in all cases: 08 September 2019, 29 September 2019, 3 August 2020, 7 August 2020, 2 August 2021, 5 September 2021, 13 September 2021, and 17 September 2021. Although the widths of these freeboard peaks vary by case (∼5 to ∼30 km), the locations of these peaks broadly correspond to the edges of the polynyas. Those freeboard peaks are evidence that sea ice pile-up or deformation at the edges of polynyas can be detected by satellite (also see Figures 4 and 7).

4.3. Limitation of IS2 Measurements

Although we characterize the spatiotemporal variations of thermodynamic ice growth, sea ice advection, and sea ice deformation by taking advantage of the fine resolution of the IS2 satellite altimeter, it is worth mentioning some intrinsic limitations of our IS2-based approach. First, we note that the absolute value of ridge fraction could be underestimated because the resolution of the IS2 ATL10 product (∼12–15 m length of height segment) is not able to detect narrow ridges of <10 m in width (Duncan & Farrell, 2022; Farrell et al., 2020; Ricker et al., 2023). Nevertheless, the regional-scale spatiotemporal distributions of pressure ridges in the Ross Sea are successfully captured by the ATL10 product in this study.

Second, considering the along-track measurements of IS2 and its 91-day revisit cycle, IS2 cannot fully cover the entire Ross Sea within a month period. In general, two or three IS2 tracks pass the Ross Sea on a single day, and such a small number of available tracks restrict the short-term coverage area of IS2. Moreover, since the IS2 laser photons cannot penetrate clouds, the useable IS2 data can be extremely limited under cloudy conditions. Such a limited spatiotemporal coverage area can bring considerable uncertainties in representing the sea ice deformation features over the entire Ross Sea.

Finally, in order to convert the IS2 freeboard into SIT, we calculate snow depth from the total freeboard by using the linear equations proposed by Kacimi and Kwok (2020). Although the assumption of the linear relationship between snow depth and total freeboard has been accepted in other studies (Ozsoy-Cicek et al., 2013; Xu et al., 2021), the determination of snow depth is still a challenging problem in remote sensing of Antarctic SIT because of the complex conditions of snow on sea ice (e.g., flooding of snow-ice interface, slush layer between snow and ice). In particular, given that the empirical equation of Kacimi and Kwok (2020) uses the CryoSat-2 radar altimeter, there is a possibility that snow depth is underestimated and ice thickness is overestimated because of the radar penetration issue of CryoSat-2. Even though the selection of a certain snow depth retrieval method can introduce uncertainties in SIT retrieval, we find that snow depth retrievals do not have significant
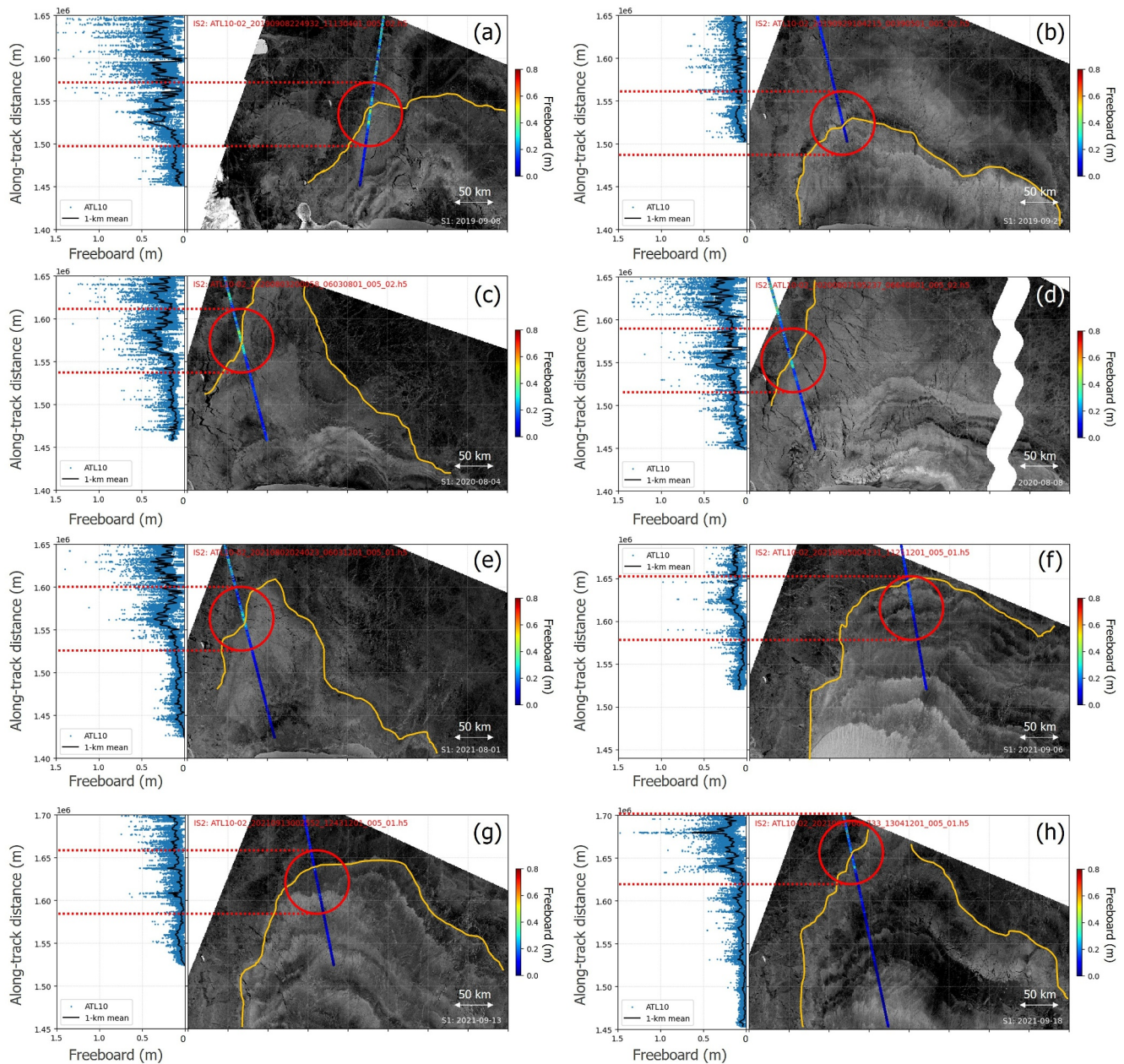
Figure 12. IS2 freeboard profiles at the polynya events on (a) 08 September 2019, (b) 29 September 2019, (c) 3 August 2020, (d) 7 August 2020, (e) 2 August 2021, (f) 5 September 2021, (g) 13 September 2021, and (h) 17 September 2021. The edges of polynyas (i.e., the outermost boundaries of polynyas) are manually drawn as yellow lines. Abrupt freeboard peaks at the polynya edges are indicated by red circles. Sentinel-1 SAR images have no more than 1 day of time difference with the coincident IS2 tracks.

impacts on describing the regional-scale spatiotemporal changes of the modal SIT (see Figures S1 and S2 in Supporting Information S1).

5. Conclusion

In this study, the ICESat-2 ATL10 sea ice freeboard product is used to characterize the spatiotemporal variations of thermodynamic and dynamic sea ice features in the Ross Sea for 4 years, from 2019 to 2022. As an indirect indicator of thermodynamic ice growth and sea ice advection, we use the modal SIT. Among four geographic sectors of the Ross Sea, the SW sector shows the lowest modal SIT for all years because katabatic winds from the

Ross Ice Shelf push away coastal sea ice and new ice forms in the large recurring polynyas. On the other hand, the SE sector shows the greatest modal SIT in October 2019/2020 due to the inflow of thick ice from the Amundsen Sea. However, the modal SIT in the SE sector decreased in the winter and spring of 2021/2022 due to the reduction of thick ice inflow from the Amundsen Sea. While the sea ice advection is the main driver for the modal SIT changes in the SW and SE sectors, the NW and NE sectors are more affected by thermodynamic ice freezing and melting. When the modal SIT is compared with the air temperature, they show significant correlations (>0.5; with p-values <0.01) in the NW and NE sectors: the decrease in air temperature leads to the increase in the modal SIT and warming air temperature leads to decrease in the modal SIT.

Each geographic sector also has distinctive characteristics in sea ice deformation. The SE shows the largest portion of sea ice deformation among the four sectors: up to >10% of ridge fraction in 2019 and 2020. Such a higher deformation is caused by the westward drift of thick ice from the Amundsen Sea. The SE sector is an intersecting area between the southerly wind from the SW sector and the easterly wind from the Amundsen Sea, where the thick ice from the Amundsen Sea is likely deformed by the convergent ice interaction. However, these deformation features disappeared in 2021 and 2022 because of the changes in wind direction caused by the deep ASL. As a result, the convergent interaction of ice floes and sea ice deformation weakened in 2021 and 2022. On the contrary, the SW and NW sectors have a low portion of pressure ridges due to the strong katabatic winds from the Ross Ice Shelf. The result of this study demonstrates that IS2 can capture the spatiotemporal changes in sea ice deformation caused by atmospheric changes.

Data Availability Statement

ICESat-2 ATL10 product is available from the National Snow and Ice Data Center: https://nsidc.org/data/atl10/versions/6 (Kwok et al., 2023). ERA5 reanalysis products are available from the Climate Data Store of the Copernicus Climate Change Service (https://cds.climate.copernicus.eu/cdsapp#!/dataset/reanalysis-era5-single-levels-monthly-means). Sentinel-1 SAR images are accessed through Google Earth Engine (https://developers.google.com/earth-engine/datasets/catalog/COPERNICUS_S1_GRD) and Alaska Satellite Facility (https://asf.alaska.edu/). Sea ice velocity data is available from the National Snow and Ice Data Center: https://nsidc.org/data/nsidc-0116/versions/4 (Tschudi et al., 2019).

References

Bell, B., Hersbach, H., Simmons, A., Berrisford, P., Dahlgren, P., Horányi, A., et al. (2021). The ERA5 global reanalysis: Preliminary extension to 1950. *Quarterly Journal of the Royal Meteorological Society*, *147*(741), 4186–4227. https://doi.org/10.1002/qj.4174

Cavalieri, D. J., & Parkinson, C. L. (1981). Large-scale variations in observed Antarctic Sea Ice extent and associated atmospheric circulation. *Monthly Weather Review*, *109*(11), 2323–2336. https://doi.org/10.1175/1520-0493(1981)109<2323:LSVIOA>2.0.CO;2

Coggins, J. H. J., McDonald, A. J., & Jolly, B. (2014). Synoptic climatology of the Ross ice Shelf and Ross Sea region of Antarctica: K-Means clustering and validation. *International Journal of Climatology*, *34*(7), 2330–2348. https://doi.org/10.1002/joc.3842

Dai, L., Xie, H., Ackley, S. F., & Mestas-Nuñez, A. M. (2020). Ice production in Ross ice Shelf polynyas during 2017–2018 from sentinel–1 SAR images. *Remote Sensing*, *12*(9), 1484. https://doi.org/10.3390/rs12091484

Dale, E. R., McDonald, A. J., Coggins, J. H. J., & Rack, W. (2017). Atmospheric forcing of sea ice anomalies in the Ross Sea polynya region. *The Cryosphere*, *11*(1), 267–280. https://doi.org/10.5194/tc-11-267-2017

DeLiberty, T. L., Geiger, C. A., Ackley, S. F., Worby, A. P., & Van Woert, M. L. (2011). Estimating the annual cycle of sea-ice thickness and volume in the Ross Sea. *Deep-Sea Research Part II Topical Studies in Oceanography*, *58*(9–10), 1250–1260. https://doi.org/10.1016/j.dsr2.2010.12.005

Dickinson, R. E., Meehl, G. A., & Washington, W. M. (1987). Ice-albedo feedback in a CO_2-doubling simulation. *Climatic Change*, *10*(3), 241–248. https://doi.org/10.1007/BF00143904

Duncan, K., & Farrell, S. L. (2022). Determining variability in Arctic Sea Ice pressure ridge topography with ICESat-2. *Geophysical Research Letters*, *49*(18), e2022GL100272. https://doi.org/10.1029/2022GL100272

Duncan, K., Farrell, S. L., Hutchings, J., & Richter-Menge, J. (2020). Late winter observations of Sea Ice pressure ridge sail height. *IEEE Geoscience and Remote Sensing Letters*, *18*(9), 1525–1529. https://doi.org/10.1109/lgrs.2020.3004724

Emanuel, P. (1962). On estimation of a probability density function and mode. *The Annals of Mathematical Statistics*, *33*(3), 1065–1076. https://doi.org/10.1214/aoms/1177704472

England, M. R., Polvani, L. M., Sun, L., & Deser, C. (2020). Tropical climate responses to projected Arctic and Antarctic sea-ice loss. *Nature Geoscience*, *13*(4), 275–281. https://doi.org/10.1038/s41561-020-0546-9

Farrell, S. L., Duncan, K., Buckley, E. M., Richter-Menge, J., & Li, R. (2020). Mapping Sea ice surface topography in high fidelity with ICESat-2. *Geophysical Research Letters*, *47*(21), e2020GL090708. https://doi.org/10.1029/2020GL090708

Gilbert, E., & Holmes, C. (2024). 2023's Antarctic sea ice extent is the lowest on record. *Weather*, *79*(2), 46–51. https://doi.org/10.1002/wea.4518

Hersbach, H., Bell, B., Berrisford, P., Hirahara, S., Horányi, A., Muñoz-Sabater, J., et al. (2020). The ERA5 global reanalysis. *Quarterly Journal of the Royal Meteorological Society*, *146*(730), 1999–2049. https://doi.org/10.1002/qj.3803

Hollands, T., & Dierking, W. (2016). Dynamics of the Terra Nova Bay polynya: The potential of multi-sensor satellite observations. *Remote Sensing of Environment*, *187*, 30–48. https://doi.org/10.1016/j.rse.2016.10.003

Kacimi, S., & Kwok, R. (2020). The Antarctic Sea ice cover from ICESat-2 and CryoSat-2: Freeboard, snow depth, and ice thickness. *The Cryosphere*, *14*(12), 4453–4474. https://doi.org/10.5194/tc-14-4453-2020

Kern, S., Ozsoy-çiçek, B., & Worby, A. P. (2016). Antarctic sea-ice thickness retrieval from ICESat: Inter-comparison of different approaches. *Remote Sensing*, *8*(7), 538. https://doi.org/10.3390/rs8070538

Koo, Y., Lei, R., Cheng, Y., Cheng, B., Xie, H., Hoppmann, M., et al. (2021a). Estimation of thermodynamic and dynamic contributions to sea ice growth in the Central Arctic using ICESat-2 and MOSAiC SIMBA buoy data. *Remote Sensing of Environment*, *267*, 112730. https://doi.org/10.1016/j.rse.2021.112730

Koo, Y., Xie, H., Kurtz, N. T., Ackley, S. F., & Mestas-Nuñez, A. M. (2021b). Weekly mapping of Sea Ice freeboard in the Ross Sea from ICESat-2. *Remote Sensing*, *13*(16), 3277. https://doi.org/10.3390/rs13163277

Kurtz, N. T., & Markus, T. (2012). Satellite observations of Antarctic sea ice thickness and volume. *Journal of Geophysical Research*, *117*(C8), C08025. https://doi.org/10.1029/2012JC008141

Kwok, R. (2010). Satellite remote sensing of sea-ice thickness and kinematics: A review. *Journal of Glaciology*, *56*(200), 1129–1140. https://doi.org/10.3189/002214311796406167

Kwok, R., Comiso, J. C., Martin, S., & Drucker, R. (2007). Ross Sea polynyas: Response of ice concentration retrievals to large areas of thin ice. *Journal of Geophysical Research*, *112*(C12), C12012. https://doi.org/10.1029/2006JC003967

Kwok, R., Cunningham, G., Hancock, D., Ivanoff, A., & Wimert, J. (2021). Algorithm Theoretical Basis Document (ATBD): Sea ice products. *1–142*. https://icesat-2.gsfc.nasa.gov/sites/default/files/page_files/ICESat2_ATL07_ATL10_ATBD_r001.pdf

Kwok, R., Kacimi, S., Markus, T., Kurtz, N. T., Studinger, M., Sonntag, J. G., et al. (2019a). ICESat-2 surface height and Sea Ice freeboard assessed with ATM Lidar acquisitions from operation IceBridge. *Geophysical Research Letters*, *46*(20), 11228–11236. https://doi.org/10.1029/2019GL084976

Kwok, R., Markus, T., Kurtz, N. T., Petty, A. A., Neumann, T. A., Farrell, S. L., et al. (2019b). Surface height and Sea Ice freeboard of the Arctic ocean from ICESat-2: Characteristics and early results. *Journal of Geophysical Research: Oceans*, *124*(10), 6942–6959. https://doi.org/10.1029/2019JC015486

Kwok, R., Petty, A. A., Cunningham, G., Markus, T., Hancock, D., Ivanoff, A., et al. (2023). ATLAS/ICESat-2 L3A Sea Ice freeboard, version 6 [Dataset]. *National Snow and Ice Data Center*. https://doi.org/10.5067/ATLAS/ATL10.006

Li, H., Xie, H., Kern, S., Wan, W., Ozsoy, B., Ackley, S., & Hong, Y. (2018). Spatio-temporal variability of Antarctic sea-ice thickness and volume obtained from ICESat data using an innovative algorithm. *Remote Sensing of Environment*, *219*(September), 44–61. https://doi.org/10.1016/j.rse.2018.09.031

Liu, J., Zhu, Z., & Chen, D. (2023). Lowest Antarctic Sea Ice record broken for the second year in a row. *Ocean-Land-Atmosphere Research*, *2*, 0007. https://doi.org/10.34133/olar.0007

Magruder, L. A., Brunt, K. M., & Alonzo, M. (2020). Early ICESat-2 on-orbit geolocation validation using ground-based corner cube retro-reflectors. *Remote Sensing*, *12*(21), 3653. https://doi.org/10.3390/rs12213653

Markus, T., Neumann, T., Martino, A., Abdalati, W., Brunt, K., Csatho, B., et al. (2017). The Ice, Cloud, and Land Elevation Satellite-2 (ICESat-2): Science requirements, concept, and implementation. *Remote Sensing of Environment*, *190*, 260–273. https://doi.org/10.1016/j.rse.2016.12.029

Marzocchi, A., & Jansen, M. F. (2017). Connecting Antarctic sea ice to deep-ocean circulation in modern and glacial climate simulations. *Geophysical Research Letters*, *44*(12), 6286–6295. https://doi.org/10.1002/2017GL073936

Massom, R. A., & Stammerjohn, S. E. (2010). Antarctic sea ice change and variability—Physical and ecological implications. *Polar Science*, *4*(2), 149–186. https://doi.org/10.1016/j.polar.2010.05.001

Morales Maqueda, M. A., Willmott, A. J., & Biggs, N. R. T. (2004). Polynya dynamics: A review of observations and modeling. *Reviews of Geophysics*, *42*(1), RG1004. https://doi.org/10.1029/2002RG000116

Neumann, T. A., Martino, A. J., Markus, T., Bae, S., Bock, M. R., Brenner, A. C., et al. (2019). The ice, cloud, and land elevation satellite – 2 mission: A global geolocated photon product derived from the advanced topographic laser altimeter system. *Remote Sensing of Environment*, *233*, 111325. https://doi.org/10.1016/j.rse.2019.111325

Nihashi, S., & Ohshima, K. I. (2015). Circumpolar mapping of Antarctic coastal polynyas and Landfast Sea ice: Relationship and variability. *Journal of Climate*, *28*(9), 3650–3670. https://doi.org/10.1175/JCLI-D-14-00369.1

Ohshima, K. I., Fukamachi, Y., Williams, G. D., Nihashi, S., Roquet, F., Kitade, Y., et al. (2013). Antarctic Bottom Water production by intense sea-ice formation in the Cape Darnley polynya. *Nature Geoscience*, *6*(3), 235–240. https://doi.org/10.1038/ngeo1738

Ohshima, K. I., Nihashi, S., & Iwamoto, K. (2016). Global view of sea-ice production in polynyas and its linkage to dense/bottom water formation. *Geoscience Letters*, *3*(1), 13. https://doi.org/10.1186/s40562-016-0045-4

Ozsoy-Cicek, B., Ackley, S., Xie, H., Yi, D., & Zwally, J. (2013). Sea ice thickness retrieval algorithms based on in situ surface elevation and thickness values for application to altimetry. *Journal of Geophysical Research: Oceans*, *118*(8), 3807–3822. https://doi.org/10.1002/jgrc.20252

Parkinson, C. L. (2019). A 40-y record reveals gradual Antarctic sea ice increases followed by decreases at rates far exceeding the rates seen in the Arctic. *Proceedings of the National Academy of Sciences of the U S A*, *116*(29), 14414–14423. https://doi.org/10.1073/pnas.1906556116

Parkinson, C. L., & Cavalieri, D. J. (2012). Antarctic sea ice variability and trends, 1979–2010. *The Cryosphere*, *6*(4), 871–880. https://doi.org/10.5194/tc-6-871-2012

Purich, A., & Doddridge, E. W. (2023). Record low Antarctic sea ice coverage indicates a new sea ice state. *Communications Earth & Environment*, *4*(1), 314. https://doi.org/10.1038/s43247-023-00961-9

Rack, W., Price, D., Haas, C., Langhorne, P. J., & Leonard, G. H. (2021). Sea ice thickness in the western Ross Sea. *Geophysical Research Letters*, *48*(1), e2020GL090866. https://doi.org/10.1029/2020GL090866

Raphael, M. N., & Handcock, M. S. (2022). A new record minimum for Antarctic sea ice. *Nature Reviews Earth & Environment*, *3*(4), 215–216. https://doi.org/10.1038/s43017-022-00281-0

Ricker, R., Fons, S., Jutila, A., Hutter, N., Duncan, K., Farrell, S. L., et al. (2023). Linking scales of sea ice surface topography: Evaluation of ICESat-2 measurements with coincident helicopter laser scanning during MOSAiC. *The Cryosphere*, *17*(3), 1411–1429. https://doi.org/10.5194/tc-17-1411-2023

Riihelä, A., Bright, R. M., & Anttila, K. (2021). Recent strengthening of snow and ice albedo feedback driven by Antarctic sea-ice loss. *Nature Geoscience*, *14*(11), 832–836. https://doi.org/10.1038/s41561-021-00841-x

Stammerjohn, S. E., Martinson, D. G., Smith, R. C., & Iannuzzi, R. A. (2008). Sea ice in the western Antarctic Peninsula region: Spatio-temporal variability from ecological and climate change perspectives. *Deep Sea Research Part II: Topical Studies in Oceanography*, *55*(18), 2041–2058. https://doi.org/10.1016/j.dsr2.2008.04.026

Tamura, T., Ohshima, K. I., & Nihashi, S. (2008). Mapping of sea ice production for Antarctic coastal polynyas. *Geophysical Research Letters*, *35*(7), L07606. https://doi.org/10.1029/2007GL032903

Tin, T., & Jeffries, M. O. (2003). Morphology of deformed first-year sea ice features in the Southern Ocean. *Cold Regions Science and Technology*, *36*(1), 141–163. https://doi.org/10.1016/S0165-232X(03)00008-9

Toggweiler, J. R., & Samuels, B. (1995). Effect of Sea Ice on the salinity of Antarctic bottom waters. *Journal of Physical Oceanography*, *25*(9), 1980–1997. https://doi.org/10.1175/1520-0485(1995)025<1980:EOSIOT>2.0.CO;2

Tschudi, M., Meier, W. N., Stewart, J. S., Fowler, C., & Maslanik, J. (2019). *Polar pathfinder daily 25 km EASE-grid Sea Ice motion vectors version 4 NASA national snow and ice data*. Center Distributed Active Archive Center. https://doi.org/10.5067/INAWUWO7QH7B

Turner, J., Holmes, C., Caton Harrison, T., Phillips, T., Jena, B., Reeves-Francois, T., et al. (2022). Record low Antarctic Sea Ice cover in February 2022. *Geophysical Research Letters*, *49*(12), e2022GL098904. https://doi.org/10.1029/2022GL098904

Van Woert, M. L. (1999). Wintertime dynamics of the Terra Nova Bay polynya. *Journal of Geophysical Research*, *104*(C4), 7753–7769. https://doi.org/10.1029/1999JC900003

Wang, J., Luo, H., Yang, Q., Liu, J., Yu, L., Shi, Q., & Han, B. (2022). An unprecedented record low Antarctic sea-ice extent during Austral summer 2022. *Advances in Atmospheric Sciences*, *39*(10), 1591–1597. https://doi.org/10.1007/s00376-022-2087-1

Williams, G., Maksym, T., Wilkinson, J., Kunz, C., Murphy, C., Kimball, P., & Singh, H. (2015). Thick and deformed Antarctic sea ice mapped with autonomous underwater vehicles. *Nature Geoscience*, *8*(1), 61–67. https://doi.org/10.1038/ngeo2299

Wingham, D. J., Francis, C. R., Baker, S., Bouzinac, C., Brockley, D., Cullen, R., et al. (2006). CryoSat: A mission to determine the fluctuations in Earth's land and marine ice fields. *Advances in Space Research*, *37*(4), 841–871. https://doi.org/10.1016/j.asr.2005.07.027

Worby, A. P., Jeffries, M. O., Weeks, W. F., Morris, K., & Jaña, R. (1996). The thickness distribution of sea ice and snow cover during late winter in the Bellingshausen and Amundsen Seas, Antarctica. *Journal of Geophysical Research*, *101*(C12), 28441–28455. https://doi.org/10.1029/96JC02737

Xie, H., Ackley, S. F., Yi, D., Zwally, H. J., Wagner, P., Weissling, B., et al. (2011). Sea-ice thickness distribution of the Bellingshausen Sea from surface measurements and ICESat altimetry. *Deep Sea Research Part II: Topical Studies in Oceanography*, *58*(9), 1039–1051. https://doi.org/10.1016/j.dsr2.2010.10.038

Xie, H., Tekeli, A. E., Ackley, S. F., Yi, D., & Zwally, H. J. (2013). Sea ice thickness estimations from ICESat altimetry over the Bellingshausen and Amundsen Seas, 2003–2009. *Journal of Geophysical Research: Oceans*, *118*(5), 2438–2453. https://doi.org/10.1002/jgrc.20179

Xu, Y., Li, H., Liu, B., Xie, H., & Ozsoy-Cicek, B. (2021). Deriving Antarctic sea-ice thickness from satellite altimetry and estimating consistency for NASA's ICESat/ICESat-2 missions. *Geophysical Research Letters*, *48*(20), e2021GL093425. https://doi.org/10.1029/2021GL093425

Zwally, H. J., Schutz, B., Abdalati, W., Abshire, J., Bentley, C., Brenner, A., et al. (2002). ICESat's laser measurements of polar ice, atmosphere, ocean, and land. *Journal of Geodynamics*, *34*(3), 405–445. https://doi.org/10.1016/S0264-3707(02)00042-X

References From the Supporting Information

Meier, W., Markus, N. T., & Comiso, J. C. (2018). *AMSR-E/AMSR2 Unified L3 daily 12.5 km Brightness temperatures, Sea Ice concentration, motion & snow depth polar Grids, version 1*. NASA National Snow and Ice Data Center Distributed Active Archive Center. https://doi.org/10.5067/RA1MIJOYPK3P

Worby, A. P., Geiger, C. A., Paget, M. J., Van Woert, M. L., Ackley, S. F., & DeLiberty, T. L. (2008). Thickness distribution of Antarctic sea ice. *Journal of Geophysical Research*, *113*(C5), C05S92. https://doi.org/10.1029/2007JC004254